J Solid State Electrochem (2010) 14:643–650
DOI 10.1007/s10008-009-0830-5

ORIGINAL PAPER

On the pseudocapacitive behavior of nanostructured molybdenum oxide

Hossein Farsi · Fereydoon Gobal · Heidar Raissi · Shokufeh Moghiminia

Received: 26 February 2009 / Revised: 3 March 2009 / Accepted: 10 March 2009 / Published online: 28 March 2009

Abstract Nanostructured molybdenum oxide was potentiodynamically deposited onto a stainless steel surface from an aqueous bath by cycling the potential between 0 and −0.75 V vs. Ag/AgCl. The deposit consisted of particulates in the range of 30 to 80 nm. Electrochemical studies under galvanostatic charge/discharge and also impedance spectroscopy revealed capacitive behavior in the potential range of −0.3 to −0.55 V vs. Ag/AgCl with the value of 477 F g^{-1} at 0.1 mA/cm^2. An equivalent circuit comprising of three parallel branches consisting of double-layer capacitance, Warburg impedance, and a constant phase element signifying pseudo-capacitance each coupled with their corresponding resistances was fitted to the experimental findings, and the magnitudes of the elements were derived.

Keywords Molybdenum oxide · Nanostructure · Pseudocapacitive behavior · Impedance spectroscopy

Introduction

Electrochemical capacitors have attracted increased interest due to their higher-power density and long life cycle compared to batteries and higher energy density compared to conventional capacitors [1]. According to charge storage mechanisms, they are categorized into two major groups: Electrochemical Double Layer Capacitors (EDLCs) with a double-layer charging mechanism and Faradaic capacitors or pseudocapacitors which a Faradaic reaction is responsible for the storage of charge. Carbonaceous materials are well-known substances that make EDLCs while conducting polymers and transition metal oxides are good candidates as electrode materials for pseudocapacitors due to their variable valences. A capacitance as high as 780 F/g has been reported for a sol–gel prepared hydrated ruthenium oxide by Zheng et al. [2], but the cost and poisoning nature of ruthenium oxide are the major drawbacks for its industrial applications. Therefore, recent researches have been focused on substituting it completely or partially by other metal oxides. So far, MnO_x [3–5], CoO_x [6, 7], and NiO_x [8, 9] have been studied widely, but there are a few reports on the capacitive behaviors of molybdenum oxide against the different valences of molybdenum [10, 11].

On the other hand, transition metal oxides are suitable materials for small ions, like H^+ and Li^+, intercalation/deintercalation, a process which makes them suitable for a wide range of applications such as uses in electrochromic and energy-storage devices. Among metal oxides, molybdenum oxide seems a promising candidate for such applications due to different oxidation states of molybdenum [12].

Molybdenum oxide is a wide band gap n-type semiconductor which plays an important role in technological applications because of its structural and electronic properties. Molybdenum oxide thin film is applied as gas sensor for different gases like NO, NO_2, CO, H_2, and NH_3 [13, 14]. Also, when molybdenum oxide is irradiated with UV light, its color changes, and this property has a wide range of displaying applications from large area display screens to smart windows [15, 16]. Due to its crystal structure,

This paper has been presented in: The Second international conference on nanoscience and nanotechnology, Tabriz, Iran, October 2009

H. Farsi (✉) · H. Raissi · S. Moghiminia
Department of Chemistry, University of Birjand,
P.O. Box 97175-615, Birjand, Iran
e-mail: hofarsi@birjand.ac.ir

F. Gobal
Department of Chemistry, Sharif University of Technology,
P.O. Box 11365-9516, Tehran, Iran

molybdenum oxide has widely used as cathode materials for lithium ion batteries [17–19].

So far, molybdenum oxide has been prepared by different methods like chemical vapor deposition [20], sol–gel [21], hydrothermal decomposition [22, 23], electrospinning [24], electrodeposition [25–31], and so on. Among these methods, electrodeposition technique sounds to be the most economic and suitable for making thin films due to its low energy consumption and good sticking to a conducting supports.

In this study, we prepared nanostructured molybdenum oxide by potentiodynamic electrodeposition onto stainless steel and investigated its pseudocapacitive behavior by cyclic voltammetry, galvanic charge/discharge, and impedance spectroscopy in a solution of $H_2SO_4 + Na_2SO_4$. To the best of our knowledge, there is no report on the study of nanostructured molybdenum oxide prepared by electrodeposition onto commercial stainless steel in such solution.

Experimental

Nanostructured molybdenum oxide preparation

A commercial grade stainless steel (grade 304) was cut into the given size (1×10 cm). The obtained stainless steel was polished with emery paper to a rough finish, washed free of emery particles in dilute nitric acid solution, and then water and the air-dried. H_2SO_4, Na_2MoO_4, and Na_2SO_4 were Merck products and were used without further purifications. All solutions were prepared using double distilled water. A standard three-electrode cell was used both for deposition and characterization experiments in which the (coated) stainless steel sheet, a platinum grid, and a saturated Ag/AgCl electrode were used as a working, counter, and reference electrode, respectively.

The electrodeposition bath was prepared by dissolving appropriate amounts of Na_2MoO_4 and H_2SO_4 in double distilled water to have a solution of 0.04 M Na_2MoO_4 and 0.01 M H_2SO_4. Molybdenum oxide was potentiodynamically electrodeposited onto the 1 cm^2 area tip of a stainless steel at room temperature. Subsequent to deposition, the obtained electrode was washed in distilled water and then used in electrochemical test solution; hereafter, we will call it as-deposited nanostructured molybdenum oxide (ANMO). The color of as-deposited film was yellowish brown.

Characterization of as-deposited nanostructured molybdenum oxide

The X-ray diffraction pattern of as-deposited materials was obtained by means of Philips X-ray diffractometer (Model PW 1840) using Cu K_α radiation in the range of scanning angle 20–80 (2θ). Surface morphological studies were carried out with scanning probe micrographs, obtained with a Dual Scope SPM (DME, Denmark). The amount of molybdenum oxides in the film was measured by dissolving of the film and the analysis by atomic adsorption spectroscopy, by means of AVANTA AAS (model PM). Electrodeposition, cyclic voltammetry, and galvanostatic charge/discharge tests were performed by a Solartron Electrochemical interface SI1287. Electrochemical impedance spectroscopy studies were carried out by a Solartron Phase Gain Analyzer SI 1260. The electrochemical tests were performed in a solution of 0.005 M H_2SO_4 and 0.095 M Na_2SO_4 at room temperature.

Results and discussion

Electrodeposition of nanostructured molybdenum oxide film

It is known that the chemical equilibrium involving molybdate ions in aqueous solutions are greatly influenced by pH and concentration. In solutions of basic or neutral pH, the major solution component is molybdate ion, MoO_4^{-2} [32], whereas in our experimental conditions, which the average degree of protonation of all species is around 0.5 [33], heptamolybdate anion, $Mo_7O_{24}^{-6}$, is the major component via the following reaction:

$$7MoO_4^{-2} + 8H^+ \rightleftarrows Mo_7O_{24}^{-6} + 4H_2O \quad (1)$$

The potentiodynamic deposition was carried out by cycling the potential between 0 to −0.75 V vs. Ag/AgCl with a potential sweep rate of 300 mV s^{-1} where 300 cycles were found to be sufficient. During the potential scanning, several reduction processes may happen and lower valences of molybdenum oxide like MoO_2, Mo_2O_5, and Mo_3O_8 are produced [34–36].

Also, at more negative potential, hydrogen insertion into molybdenum oxide occurs to form bronzes [35, 37], like:

$$MoO_{3(S)} + H_3O^+ + e^- \rightleftarrows MoO_2OH \cdot H_2O \quad (2)$$

$$Mo_3O_{8(S)} + H_3O^+ + e^- \rightleftarrows Mo_3O_7OH \cdot H_2O \quad (3)$$

Therefore, it is conceivable that electrodeposited material be a mixed valence molybdenum oxides. Dong and Wang [38] and Liu et al. [39] have reported mixed-valence molybdenum oxide film grown on carbon substrate by electrodeposition.

X-ray diffractometry

The X-ray pattern of as-deposited molybdenum oxide did not show any peaks with regard to the amorphous structure

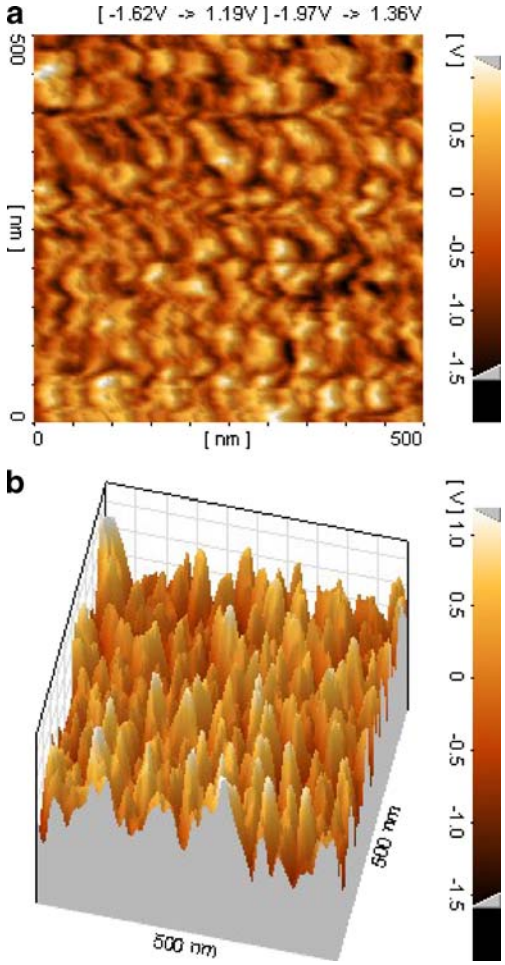

Fig. 1 **a** Two- and **b** three-dimensional scanning probe micrographs of as-deposited nanostructured molybdenum oxide, ANMO

of deposited molybdenum oxide. McEvoy and Stevenson [35, 40] and McEvoy et al. [41] have reported formation of amorphous molybdenum oxides by electrodeposition method in temperatures below 100°C.

SPM studies

To investigate the morphology of as-deposited molybdenum oxide, we used scanning potential microscopy in noncontact mode. Figure 1 illustrates the two- and three-dimensional images of as-deposited molybdenum oxide. The SPM studies show that as-deposited molybdenum oxide has a nanostructure with round grains ranging from 30 to 80 nm in diameter.

Cyclic voltammetry studies

Cyclic voltammograms of the as-deposited molybdenum oxide films in 0.005 M H_2SO_4 + 0.095 M Na_2SO_4 solution were recorded between 0 and −0.55 V at scan rates of 2, 4, and 6 mV/s. The results are presented in Fig. 2. In the cathodic half-cycle hydrogen, ion adsorption takes place and proton desorption occurs in the reverse cycle, namely:

$$\mathrm{MoO_x}\cdot y\mathrm{H_2O} + \delta\mathrm{H^+} + \delta\,\overline{\mathrm{e}} \underset{\text{Discharge}}{\overset{\text{Charge}}{\rightleftharpoons}} \mathrm{MoO_{x-\delta}(OH)_\delta}\cdot y\mathrm{H_2O} \tag{4}$$

The above Faradaic reaction is likely accompanied by charging electrical double layer and hydrogen ion diffusion to the surface and into the bulk of molybdenum oxide. Although cyclic voltammograms do not have rectangular shapes as those which have been reported for RuO_2 [42], they depict the capacitive behaviors due to nonzero cathodic and anodic currents. It means the capacity for such systems will depend on potential because of the dependency of both the cathodic and anodic currents to potential. Such behaviors have also been already reported for other metal oxides [43–45]. Due to this effect, usually, galvanostatic charge/discharge technique is used to determining of the capacitance.

Galvanostatic charge/discharge studies

The capacitive behavior of a material can be estimated by charge/discharge cycling. The specific capacitance (SC) based on charge/discharge can be calculated as follows:

$$\mathrm{SC}\left[\mathrm{F\ g^{-1}}\right] = \frac{i[\mathrm{A}] \times \Delta t[\mathrm{s}]}{\Delta E[\mathrm{V}] \times m[\mathrm{g}]} \tag{5}$$

where i is current, Δt is charging/discharging time, ΔE is change in potential during charge/discharge process, and m is mass of the active material. Figure 3 depicts the galvanic charging and discharging curves of the as-deposited

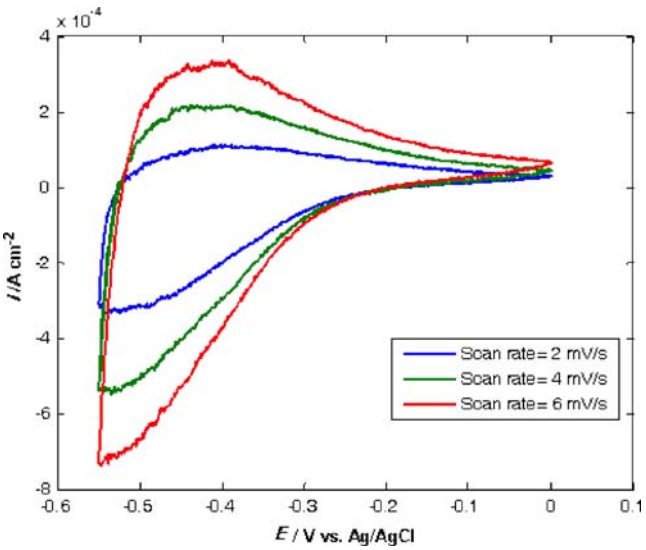

Fig. 2 Cyclic voltammograms of ANMO in 0.005 M H_2SO_4+ 0.095 M Na_2SO_4 at different scan rates

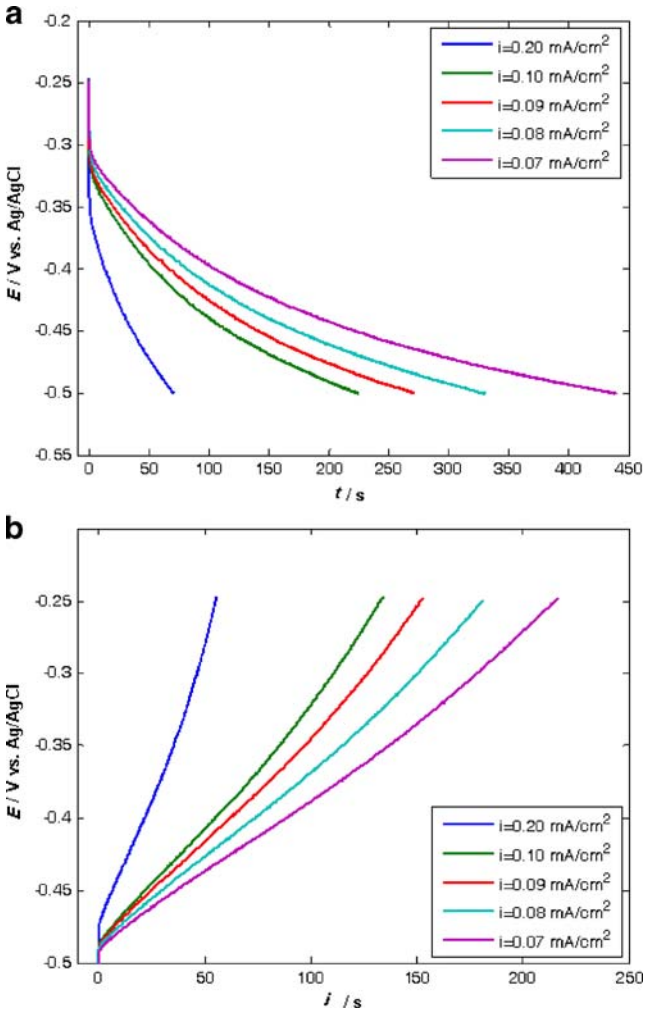

Fig. 3 Galvanic **a** charge and **b** discharge curves of ANMO in 0.005 M H_2SO_4+0.095 M Na_2SO_4 at different constant currents

molybdenum oxide between −0.25 and −0.50 V vs. Ag/AgCl at different constant currents. By increasing the applied current, both charging and discharging times decrease. However, charging and discharging processes do not show a symmetric behavior pointing to asymmetric behavior of anodic and cathodic regions of cyclic voltammograms. In fact, a sharp potential change is observed at the initial stages of discharge which have been related to both Ohmic and kinetic resistance [46–48]. Therefore, the potential change during discharge has two parts, a linear sharp change region, ΔE_1, and a moderate nonlinear potential change region, ΔE_2, [49] which is responsible for the pseudo-capacity of the active electrode materials. Due to this nonlinear change in potential vs. time, ΔE in Eq. 8 should take an average value [46–48] as calculated through:

$$\Delta E_{\text{ave}} = \frac{1}{\Delta t}\int_{t_1}^{t_2} E\mathrm{d}t \tag{6}$$

Specific capacitances have been calculated using galvanostatic discharge curves (Fig. 3b and Eqs. 9 and 10 and have been shown in Table 1). As these data show, discharge capacitance decreases by increasing the withdrawing cell current because the slower Faradaic processes cannot participate in providing charge at the interface to be removed at larger cell current. In another words, there is a kinetic resistance which enhances by increasing in cell current. Figure 3 also points to the fact that the kinetics of charge is considerably slower than the discharging process as signified by longer charge times. The process of proton (ion) insertion/de-insertion into the bulk of molybdenum oxide is, thus, conceivable.

Table 1 The discharge capacity of ANMO at different withdrawing cell currents

i/mAcm^{-2}	Specific capacitance/F g^{-1}
0.2	428.8
0.1	477.0
0.09	524.2
0.08	548.8
0.07	565.3

Chronoamperometric studies

To illustrate dependency of hydrogen ion adsorption/insertion onto the ANMO, we applied different negative potential to the electrode and followed the current response as a function of time. Figure 4 depicts chronoamperograms of ANMO at the first 50 s of experiment. No negative current is observed above −0.3 V vs. Ag/AgCl. However, a negative current appears at more negative potentials with its amount increasing at more negative potentials. All chro-

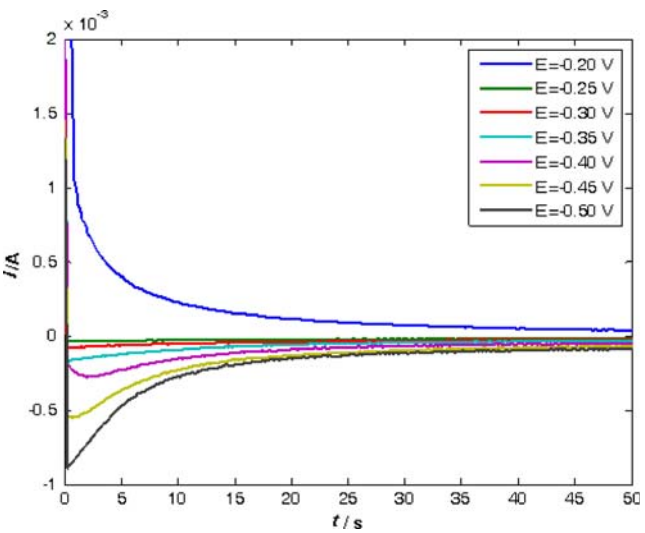

Fig. 4 Chronoamperograms of ANMO in 0.005 M H_2SO_4+0.095 M Na_2SO_4 at different potentials vs. Ag/AgCl reference electrode

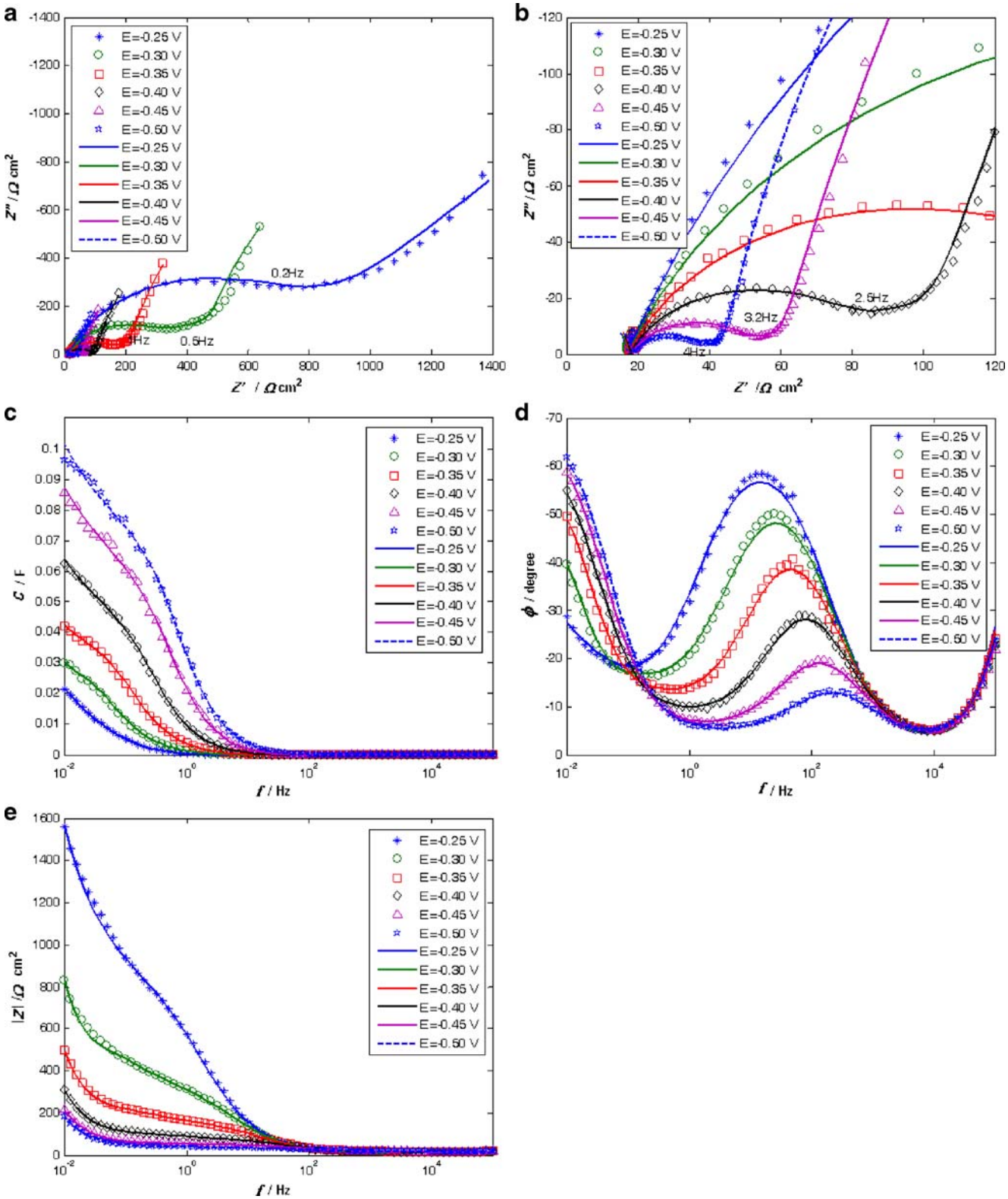

Fig. 5 **a**, **b** Nyquist plots of ANMO in 0.005 M H_2SO_4+.095 M Na_2SO_4 at different potentials. The characteristic knee frequency has been shown. Frequency dependence of the **c** capacitance, **d** phase angle, and **e** magnitude $|Z|$. The *solid lines* represent the fitted data to equivalent circuit Fig. 6

Table 2 The specific capacitance of ANMO at different potentials

E/V vs. Ag/AgCl	Specific capacitance/F g^{-1}
−0.30	113.8
−0.35	158.9
−0.40	236.2
−0.45	323.2
−0.50	364.3

noamperograms show a sharp drop at the initial stages of the experiments due to electrochemical adsorption of cations on the molybdenum oxide surface. This is followed by a slowly falling current likely supplied by charge and mass transfer processes.

Electrochemical impedance spectroscopy studies

The complex–plane impedance (Nyquist plots) and dependency of impedance magnitude, phase angle, and capacitance (Bode plots) at different potentials for ANMO have been presented in Fig. 5a–d. The capacitance was calculated from frequency dependency of imaginary part of the impedance, Z'', by using the equation:

$$C \frac{1}{2\pi f Z''} \tag{7}$$

The Nyquist plots exhibit a line with a slope close to 90° along the imaginary axis (Z'') when $E<-0.30$ V vs. Ag/AgCl. The deviation from the straight line along the imaginary axis is related to nonideally polarizable electrode (leaking capacitor) [50]. This deviation is attributed to redox-related capacitance due to proton diffusion [50]. However, at more negative potentials, $E\leq-0.55$ V vs. Ag/AgCl, the straight line was replaced by a semicircle behavior (has not been shown in the figure) which can be related to a noncapacitive Faradaic reaction, probably hydrogen evolution. In fact, hydrogen bubbles were observed on the surface of the molybdenum oxide electrode at $E\leq-0.60$ V vs. Ag/AgCl. Also, no capacitive behavior was observed at more positive of −0.2 V vs. Ag/AgCl in agreement with the CV results where no current has been witnessed, Fig. 2, and chronoamperometeric studies which do not show any negative current for hydrogen adsorption/insertion (Fig. 4).

Sugimoto et al. have separated the Bode plots into three regions, namely the high frequency, medium frequency, and low frequency regions [50] to categorize the processes which are influencing the impedance response. Briefly, at high frequency region, $|Z|$, is virtually independent of frequency, and the capacitance is nearly zero. The lower limit of high frequency region is characterized by knee frequency in the complex–plane plots. In fact, at frequencies higher than the knee frequency, fast process like charge transfer process at the surface of the electrode in contact with electrolyte (double-layer charging) will be dominant, and mass transfer can be neglected. The low frequency region is defined as the region where the $f-|Z|$ plot exhibits a slope close to −1, and $-90°<\phi<-45°$ in the f–ϕ plot. The near −1 slope shows that this region is typical of capacitive behavior. The frequency where $\phi=-45°$ can be recognized as the frequency response to the ideally capacitive behavior (capacitor response frequency), $f_{\phi=-45°}$. At low frequency region $\left(f \leq f_{\phi=-45°}\right)$, heterogeneous diffusion to the less accessible sites or leakage current may govern the impedance. The range of frequencies between knee frequency and capacitor response frequency make the medium frequency region where diffusion-controlled processes and distributed capacitance and resistance within the film (Warburg impedance) will dominate the impedance. As Fig. 5a shows, by going to more negative potential, the knee frequency increases. It means that double-layer charging occurs faster or double-layer charging time constant becomes smaller at more negative potentials. This is due to strong attraction forces between cations, H^+ or Na^+, and the more negatively charged molybdenum oxide surface at more negative potentials, which causes the positive charges transfer faster to the negatively charged walls. On the other hand, double-layer charging time constant inversely depends on the conductivities of solution and contacting solid matrix [46]. As we have used, the same electrolyte for all impedance measurements; it seems that the conductivity of molybdenum oxide matrix increases at more negative potentials. This idea is in accordance with results of $f-|Z|$ plots (Fig. 5d). The phase angle behavior plots (Fig. 5c) show that a pseudocapacitive behavior is observed only at $E<-0.30$ V, and the origin of capacity which has been shown in Fig. 5b should be just double-layer charging process. Maximum capacitance as measured by impedance measurements have been given in Table 2.

Finally, to find a better understanding about the parameters which are important in impedance response of ANMO, we used the equivalent circuit shown in Fig. 6. This equivalent circuit has already been used by Sugimoto

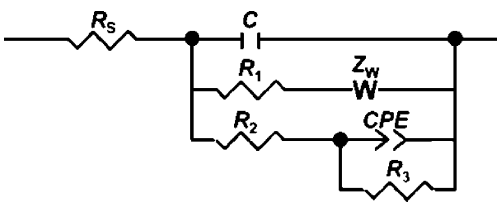

Fig. 6 The equivalent circuit used for fitting experimental results containing of three parallel branches for double-layer capacitance, Warburg impedance, and a constant phase element signifying pseudo-capacitance

Table 3 The values of some of the equivalent circuit parameters

E/V	α_{CPE}	$C_{dl}/\mu F\ cm^{-2}$	R_w/ohm cm^2	T_W/s	α_W	R_{CT}/ohm cm^2
−0.30	0.78	0.652	679.7	80.2	0.47	381.9
−0.35	0.77	0.439	227.8	43.3	0.45	187.0
−0.40	0.76	0.666	74.4	20.7	0.43	98.1
−0.45	0.73	1.028	28.3	10.3	0.44	61.0
−0.50	0.68	1.190	18.4	7.8	0.45	46.4

et al. [50] to investigate the response of hydrated ruthenium oxide in 10 M H_2SO_4. Briefly, a Randles type circuit, $R_S(C_{dl}(R_1Z_W))$, was found to simulate well the high- and medium-frequency experimental data, where R_S is the solution resistance, C_{dl} is the double-layer capacitance, and Z_W is the finite length Warburg impedance. The impedance of the double-layer capacitance can be expressed as

$$Z_C = \frac{1}{i\omega C_{dl}} \tag{8}$$

where $i = \sqrt{-1}$ ω is the angular frequency. The Warburg impedance, Z_W, can be expressed as [50]

$$Z_W = \frac{R_W \coth[(iT_W\omega)^{\alpha_W}]}{(iT_W\omega)^{\alpha_W}} \tag{9}$$

where R_W is the diffusion resistance (Warburg resistance), T_W is equal to $\frac{L^2}{D}$, where is L and D are the effective diffusion length and diffusion coefficient, respectively. T_W is sometimes called diffusion time constant and α_W is a fractional exponent between 0 and 1. To account for low frequency Faradaic impedance, an additional R_2 (R_3CPE) circuit was connected in parallel to the above-mentioned circuit. A constant phase element (CPE) was used instead of a capacitor to account for heterogeneity of the surface and then capacitance dispersion. The theories attempting to rationalize capacitance dispersion consider two origins for this phenomenon; surface roughness and interfacial origins or the kinetic consequences of chemical inhomogeneities [51]. The impedance of the CPE can be expressed as [50]:

$$Z_{CPE} = \frac{1}{T_{CPE}(i\omega)^{\alpha_{CPE}}} \tag{10}$$

where T_{CPE} is the pseudocapacitance, $C_{\phi,\ \text{when}\ \alpha_{CPE}=1}$, and α_{CPE} is the constant phase element exponent ($0 \leq \alpha_{CPE} \leq 1$). Experiments done on various solid metallic electrodes have shown the smoother the surface the closer is the value of α_{CPE} to unity, i.e., the closer to ideal capacitive behavior [51]. The total impedance of equivalent circuit (Fig. 6) can be written as:

$$Z_{total} = R_s + \frac{1}{\frac{1}{Z_C} + \frac{1}{R_1+Z_W} + \frac{1}{R_2+\frac{1}{\frac{1}{R_3}+\frac{1}{Z_{CPE}}}}} \tag{11}$$

This equivalent circuit was found to fit to the experimental data very well (solid lines in Fig. 5a–d), and some of derived parameters have been presented in Table 3. As these data show, the more the negative potentials are, the larger is the deviation of α_{CPE} from unity. It means that a more capacitance dispersion exists. Because we use the same electrode at all potentials, it sounds only the interfacial phenomena govern on the CPE behavior. This is due to more cationic adsorption (a Faradaic process) at more negative potentials. This idea is in accord with charge transfer resistance changes with potential. Data of Table 3 depict that charge transfer resistance has a potential dependency, and at more negative potential, it has a smaller value due to more cationic adsorption with regard to chronoamperometric experiments (Fig. 4). Changes of diffusion parameters with potential seem so interesting. First of all, α_W has a value near to 0.5 with regard to finite length diffusion character. Both the diffusion resistance and diffusion time constant decreases by going to more negative potentials because of more facile traveling of ions inside the smaller pores.

Conclusion

The as-deposited nanostructured molybdenum oxide on stainless steel exhibits a pseudocapacitive behavior at potentials more cathodic of −0.3 V vs. Ag/AgCl. The capacitance increases by going to more negative potential due to more cationic adsorption and more facile transference of ions inside the smaller pores.

References

1. Conway BE, Supercapacitors E (1999) Scientific fundamentals and technological applications. Kluwer Academic/Plenum, New York
2. Jow TR, Zheng J (1998) J Electrochem Soc 142:49
3. Zolfaghari A, Ataherian F, Ghaemi M, Gholami A (2007) Electrochim Acta 52:2806
4. Ghaemi M, Ataherian F, Zolfaghari A, Jafari SM (2008) Electrochim Acta 53:4607
5. Subramanian V, Zhu H, Vajtai R, Ajayan PM, Wei B (2005) J Phys Chem B 109:20207
6. Lin C, Ritter JA, Popov BN (1998) J Electrochem Soc 145:4097

7. Liu TC, Pell WG, Conway BE (1999) Electrochim Acta 44:2829
8. Nam KW, Kim KB (2002) J Electrochem Soc 149:A346
9. Xu MW, Bao SJ, Li HL (2007) J Solid State Electrochem 11:372
10. Sugimoto W, Ohnuma T, Murakami Y, Takasu Y (2001) Electrochem Solid State Lett 4:A145
11. Murugan AV, Viswanath AK (2006) J App Phys 100:074319
12. Bailar JC, Emeléus HJ, Nyholm SR, Trotman-Dickenson AF (eds) (1973) Comprehensive inorganic chemistry vol 3. Pergamon Press Ltd, Oxford
13. Ferroni M, Guidi V, Martinelli G, Sacerdoti M, Nelli P, Sberveglieri G (1998) Sensor Actuator B 48:285
14. Imawan C, Steffes H, Solzbacher F, Obermeier E (2001) Sensor Actuator B 78:119
15. Pichat P, Mozzanega M, Hoang-Van C (1988) J Phys Chem 92:467
16. He T, Ma Y, Cao Y, Jiang P, Zhang X, Yang W, Yao J (2001) Langmuir 17:8024
17. Shembel E, Apostolova R, Nagirny V, Kirsanova I, Ph G, Lytvyn P (2005) J Solid State Electrochem 9:96
18. Yebka B, Julien C, Nazri GA (1999) Ionics 5:236
19. Christian PA, Carides JN, DiSalvo FJ, Waszczak V (1980) J Electrochem Soc 127:2315
20. Ivanova T, Gesheva KA, Szekeres A (2002) J Solid State Electrochem 7:21
21. Jiebing S, Rui X, Shimin W, Wufeng T, Hua T, Jing S (2003) J Sol–gel Sci Technol 27:315
22. Komaba S, Kumagai N, Kumagai R, Kumagai N, Yashiro H (2002) Solid State Ionics 152–153:319
23. Tran MH, Ohkita H, Mizushima T, Kakuta N (2005) Appl Catal, A Gen 287:129
24. Li S, Shao C, Liu Y, Tang S, Mu R (2006) J Phys Chem Solids 67:1869
25. McEvoy TM, Stevenson KJ (2003) Langmuir 19:4316
26. Pathan HM, Min SK, Jung KD, Joo OS (2006) Electrochem Commun 8:273
27. Guerfi A, Dao LH (1989) J Electrochem Soc 136:2435
28. Nagirnyi VM, Apostolova RD, Baskevich AS, Shembel EM (2004) Russ J Appl Chem 77:71
29. Więcek B, Twardoch U (2004) J Phys Chem Solids 65:263
30. Nagirnyi VM, Apostolova RD, Shembel EM (2006) Russ J Appl Chem 79:1438
31. Patil RS, Uplane MD, Patil PS (2006) Appl Surf Sci 252:8050
32. Tytko KH, Gras D (1989) Molybdenum. In: Katscher H, Schroder F (eds) Gmelin handbook of inorganic chemistry, supplement vol B3b. Springer-Verlag, New York
33. Cruywagen JJ (2000) Protonation, oligomerization, and condensation reactions of vanadate (V), molybdate (VI), and tungstate (VI). In: Sykes AG (ed) Advances in inorganic chemistry, vol 49. Academic Press, New York, pp 127–182
34. McEvoy TM, Stevenson KJ (2003) http://hdl.handle.net/2152/768
35. McEvoy TM, Stevenson KJ (2004) J Mater Res 19:429
36. Shembel E, Apostolova R, Nagriny V, Kirsanova I, Ph G, Lytvyn P (2005) J Solid State Electrochem 9:96
37. DeSmet DJ, Ord JL (1987) J Electrochem Soc 134:1734
38. Dong S, Wang B (1994) J Electroanal Chem 370:141
39. Liu S, Zhang Q, Wang E, Dong S (1999) Electrochem Commun 1:365
40. McEvoy TM, Stevenson KJ (2003) Anal Chim Acta 496:39
41. McEvoy TM, Stevenson KJ, Hupp JT, Dang X (2003) Langmuir 19:4316
42. Joe TR, Zheng JP (1998) J Electrochem Soc 145:49
43. Gupta V, Gupta S, Miura N (2008) J Power Sources 175:680
44. Luo JM, Gao B, Zhang XG (2008) Mater Res Bull 43:1119
45. Su LH, Zhang XG, Liu Y (2008) J Solid State Electrochem 12:1129
46. Lin C, Ritter JA, Popov BN, White RE (1999) J Electrochem Soc 146:3168
47. Farsi H, Gobal F (2007) J Solid State Electrochem 11:1085
48. Farsi H, Gobal F (2009) J Solid State Electrochem 13:433
49. Pico F, Ibañez J, Centeno TA, Pecharroman C, Rojas RM, Amarilla JM, Rojo JM (2006) Electrochim Acta 51:4693
50. Sugimoto W, Iwata H, Yokoshima K, Murakami Y, Takasu Y (2005) J Phys Chem B 109:7330
51. Pajkossy T (1994) J Electroanal Chem 364:111